

Article

Overcoming Challenges in Development of Manganese Oxide Supercapacitor Cathodes by Alkali-Free Hydrothermal Synthesis

Mahmoud Awad ¹, Mohamed Nawwar ² and Igor Zhitomirsky ^{1,*}

¹ Department of Materials Science and Engineering, McMaster University, Hamilton, ON L8S 4L7, Canada; awadm11@mcmaster.ca

² Technical Research Center (TRC), Cairo 11759, Egypt; nawwarm@mcmaster.ca

* Correspondence: zhitom@mcmaster.ca

Abstract: This investigation is motivated by the need in the development of manganese oxide cathodes for supercapacitors with high capacitance at high charge–discharge rates and enhanced capacitance retention in a wide range of charge–discharge rates. It also addresses the challenge of eliminating the time-consuming activation procedure, which limits the applications of Mn_3O_4 cathodes. The new approach is based on the use of environmentally friendly and biocompatible pH modifiers–dispersants, such as polyethylenimine (PEI) and meglumine (MG) for hydrothermal synthesis. In this approach, the use of inorganic alkalis is avoided. We demonstrate the benefits of this approach for the fabrication of manganese oxide nanoparticles, such as Mn-PEI and Mn-MG. Electrodes with a high active mass of 40 mg cm^{-2} are fabricated and electrochemically tested in $0.5 \text{ M Na}_2\text{SO}_4$ electrolyte. The method of electrode material fabrication offers benefits for the accelerated electrode activation procedure, which is practically eliminated for Mn-MG electrodes. The Mn-MG electrodes showed a remarkably high capacitance of 3.68 F cm^{-2} (93.19 F g^{-1}) at a sweep rate of 100 mV s^{-1} and a high capacitance retention of 90.6% in the CV sweep range of $1\text{--}100 \text{ mV s}^{-1}$.



Citation: Awad, M.; Nawwar, M.; Zhitomirsky, I. Overcoming Challenges in Development of Manganese Oxide Supercapacitor Cathodes by Alkali-Free Hydrothermal Synthesis. *Batteries* **2023**, *9*, 365. <https://doi.org/10.3390/batteries9070365>

Academic Editors: Tianming Li, Shuoqing Zhao and Leon L. Shaw

Received: 28 May 2023

Revised: 27 June 2023

Accepted: 6 July 2023

Published: 8 July 2023



Copyright: © 2023 by the authors. Licensee MDPI, Basel, Switzerland. This article is an open access article distributed under the terms and conditions of the Creative Commons Attribution (CC BY) license (<https://creativecommons.org/licenses/by/4.0/>).

1. Introduction

Wet chemical synthesis methods are widely used in the nanotechnology of redox-active materials for energy storage devices, such as batteries and supercapacitors [1,2]. New materials and methods offer excellent control of particle size on the nanometric scale and allow for the fabrication of energy storage devices with enhanced performance [1,3–7]. Such methods facilitated the doping of materials, which was a key factor for the enhancement in energy storage properties [5,8]. Hydrothermal synthesis is an important wet chemical synthesis strategy [9,10], which facilitates nanoparticle crystallization and phase control. In wet chemical synthesis methods, the pH control is usually achieved by adding alkalis, such as NaOH or KOH, to the aqueous precursor solutions of metal salts. Chemical precipitation from aqueous solutions is used for the fabrication of Mn_3O_4 for applications in supercapacitors and batteries. Synthesis is usually performed by the pH adjustment of Mn^{2+} salt solutions [11] and precipitation at $\text{pH} = 9\text{--}10$, which is significantly higher than the isoelectric point of Mn_3O_4 and other manganese oxides [12,13]. As a result, the synthesized particles are negatively charged. The synthesized particles usually form agglomerates and precipitate in agreement with the DLVO theory of colloidal stability, which predicts the coagulation of the negatively charged particles in high ionic strength solutions, containing positively charged Na^+ or K^+ ions. The prevention of nanoparticle agglomeration is important for the development of advanced Mn_3O_4 electrodes with enhanced capacitance. Despite the significant progress achieved in the development of

Mn_3O_4 electrodes, several factors limit the practical application of this material. Numerous investigations showed the need for the electrochemical activation of Mn_3O_4 electrodes and the gradual *in situ* transformation to the electrochemically active MnO_2 phase [14,15]. The important task is to accelerate or avoid the time-consuming activation cycling of such electrodes, which is necessary for achieving high capacitance [11,14,15]. Previous investigations showed that capacitance increases by three times during the activation procedure [14]. Another difficulty is related to the poor capacitance retention of Mn_3O_4 electrodes at high charge–discharge rates [14]. This limits the applications of Mn_3O_4 for the development of advanced supercapacitors with enhanced power–energy characteristics. It is hypothesized that such problems can be addressed by the development of advanced wet chemical synthesis nanotechnologies for Mn_3O_4 nanofabrication.

Our investigation is motivated by the interest in avoiding the long activation procedure and fabrication of electrodes with high capacitance at high charge–discharge rates and enhanced capacitance retention in a wide range of charge–discharge rates. Our approach is based on the use of meglumine (MG) and polyethylenimine (PEI), which strongly adsorb protons in aqueous solutions and allow for the fabrication of solutions with a high pH. We avoided the use of inorganic alkalis via the application of more environmentally friendly materials, which offer the additional benefit of enhanced nanoparticle dispersion for the fabrication of energy storage materials with enhanced performance.

The goal of this investigation was the application of MG and PEI as pH modifiers and dispersants for the hydrothermal synthesis of Mn_3O_4 nanoparticles. Proof-of-concept studies demonstrated the successful synthesis of nanoparticles, which showed good electrochemical charge storage properties for application in supercapacitors. An important finding was the ability to avoid a time-consuming electrode activation and to achieve high capacitance and excellent capacitance retention at high charge–discharge rates. The approach developed in this investigation opens a new avenue for the synthesis of other inorganic charge storage materials of different types and composites.

2. Materials and Methods

Polyethylenimine (80% ethoxylated, PEI) solution, meglumine (MG), manganese (II) nitrate tetrahydrate, polyvinyl butyral binder (PVB) supplied by Millipore Sigma (Canada) and MWCNT (OD 13 nm, ID 4 nm, length 1–2 μm) supplied by Bayer (Germany) were used. Ni foams with 95% porosity were provided by Vale (Canada). All chemicals were used without further purification.

For the preparation of the nanoparticles, a hydrothermal synthesis approach was utilized by forming 7 mM $\text{Mn}(\text{NO}_3)_2$ solution in deionized (DI) water. Then, MG or PEI was added dropwise to reach pH = 9 under constant stirring. The mixture was stirred for another two hours to complete the reaction. The resultant mixture was transferred to an 80 mL Teflon liner in a stainless-steel autoclave and left for 12 h at 150 °C.

The resulting materials were washed repetitively with DI water and ethanol to neutralize the pH and afterward left to dry for 12 h at 55 °C in an oven. For electrode fabrication, the mass ratio of Mn_3O_4 : MWCNT: PVB binder in the prepared ethanol slurry was 80:20:3. MWCNT were utilized as conductive additives. The Ni foam current collectors were impregnated with the slurry. The relatively small length of the selected MWCNT facilitated impregnation of the current collectors. The mass loading of the impregnated material after drying was 40 mg cm^{-2} . The impregnated Ni foam electrodes were compressed to 37% of the original thickness to enhance the electrical contact of the active material with Ni current collector.

The Biologic potentiostat (SP 300) was utilized to conduct all electrochemical evaluations, such as cyclic voltammetry (CV), galvanostatic charge–discharge (GCD), and electrochemical impedance spectroscopy (EIS). Aqueous 0.5 M Na_2SO_4 electrolyte was used in a three-electrode cell, with the impregnated Ni foam as a working electrode, a platinum mesh as a counter electrode, and a saturated calomel electrode (SCE) as a reference. The active area of the working electrode was 1 cm^2 . The electrochemical measurements

were used for the analysis of capacitive behavior from the integral area of CV or GCD data, as it was described in the literature [16–18]. Areal (C_S) and specific (C_m) capacitances were calculated from the CV, GCD, and EIS testing results [19]. The integral capacitances (C_S and C_m) in a potential range of 0–0.9 V were calculated using Equations (1) and (2) by normalizing the total capacitance (C) by electrode area and mass, respectively. For cyclic voltammetry:

$$C = \frac{Q}{V_{max}} = \frac{\left| \int_{t(V_0)}^{t(V_{max})} idt \right| + \left| \int_{t(V_{max})}^{t(V_0)} idt \right|}{2V_{max}} \quad (1)$$

where Q is a total charge, derived from the CV area, V_0 is an electrode potential at the beginning or end of the charge/discharge proves ($V_0 = 0$ V vs SCE) and V_{max} is the highest electrode potential during cycling ($V_{max} = 0.9$ V vs SCE), i -is current, and t is time. For galvanostatic charge–discharge:

$$C = \frac{it}{V_{max}} \quad (2)$$

Complex impedance $Z^*(\omega) = Z'(\omega) + iZ''(\omega)$ data obtained at a voltage amplitude of 5 V and different frequencies (ω) were used for the calculation of complex capacitance components $C^*(\omega) = C'(\omega) - iC''(\omega)$:

$$C' = \frac{-Z''(\omega)}{\omega |Z(\omega)|^2} \quad (3)$$

$$C'' = \frac{Z'(\omega)}{\omega |Z(\omega)|^2} \quad (4)$$

Cycling procedure (CP) involved cycling at sweep rates of 1, 5, 10, 20, 50, and 100 mV s⁻¹. EIS measurements were performed after each CP. CV and EIS measurements were repeated 5 times for the investigation of electrode activation. GCD testing was performed after 5 CPs and EIS measurements.

Transmission electron microscopy (TEM) studies were performed with a Talos L120C instrument, while scanning electron microscopy was performed using a JEOL JSM-6610 microscope. X-ray diffraction (XRD) testing was performed with a diffractometer (Bruker D8 Advance, Cu-K α radiation, UK). X-ray photoelectron spectroscopy (XPS) studies of manganese oxides prepared using MG and PEI were performed with the aid of a PHI Quantera II Scanning XPS Microprobe. The equivalent circuit simulations for EIS data were investigated using ZSimpWin software supplied by AMETEK.

3. Results and Discussion

PEI and MG were used as pH modifiers and dispersants for the synthesis of Mn-PEI and Mn-MG materials. In this approach, the use of inorganic alkalis, such as KOH or NaOH, was avoided.

The chemical structures of PEI and MG are shown in Figure 1. MG is an amino alcohol, which is derived from glucose [20]. It has previously been shown that MG is a promising biocompatible pH modifier for the solubilization of various drugs, which are insoluble in water at pH = 7, but soluble at a high pH [21–24]. The use of MG facilitated drug release [23]. The interest in biomedical applications of MG is related to its biocompatibility and biodegradability [25,26]. MG is used for the fabrication of biomedical implants and for biomedical diagnostic imaging applications [27]. Several investigations focused on applications of MG as an environmentally benign catalyst [28,29]. MG can facilitate the dispersion of inorganic particles [27]. Therefore, MG can act as a pH modifier and dispersant [27]. MG is a relatively small organic molecule, which forms aqueous solutions with pH = 11. The high pH of MG is related to proton adsorption by the NH group of this molecule. The NH and multiple OH groups of MG facilitate its adsorption on inorganic materials.

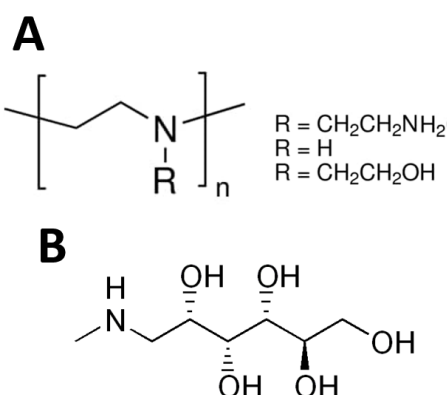


Figure 1. Chemical structures of (A) PEI and (B) MG.

PEI shows a strong adsorption of protons in water, resulting in a significant pH increase and formation of basic solutions [30]. This biocompatible polymer facilitates the dispersion of various materials [31–35]. PEI is a branched polymer, which absorbs protons from water by the protonation of amino groups. PEI formed a solution with pH = 12. Moreover, the amino groups of PEI have a strong affinity to metal atoms. As a result, PEI shows strong adsorption on the surfaces of inorganic materials. Therefore, PEI acted as a pH regulator and dispersant.

It was suggested that the adsorption of PEI and MG on inorganic surfaces during synthesis can reduce particle growth.

Hydrothermal processing resulted in successful particle synthesis in the presence of PEI and MG. Figure 2 shows the TEM images of the particles prepared by the hydrothermal synthesis in the presence of PEI (Mn-PEI) and MG (Mn-MG).

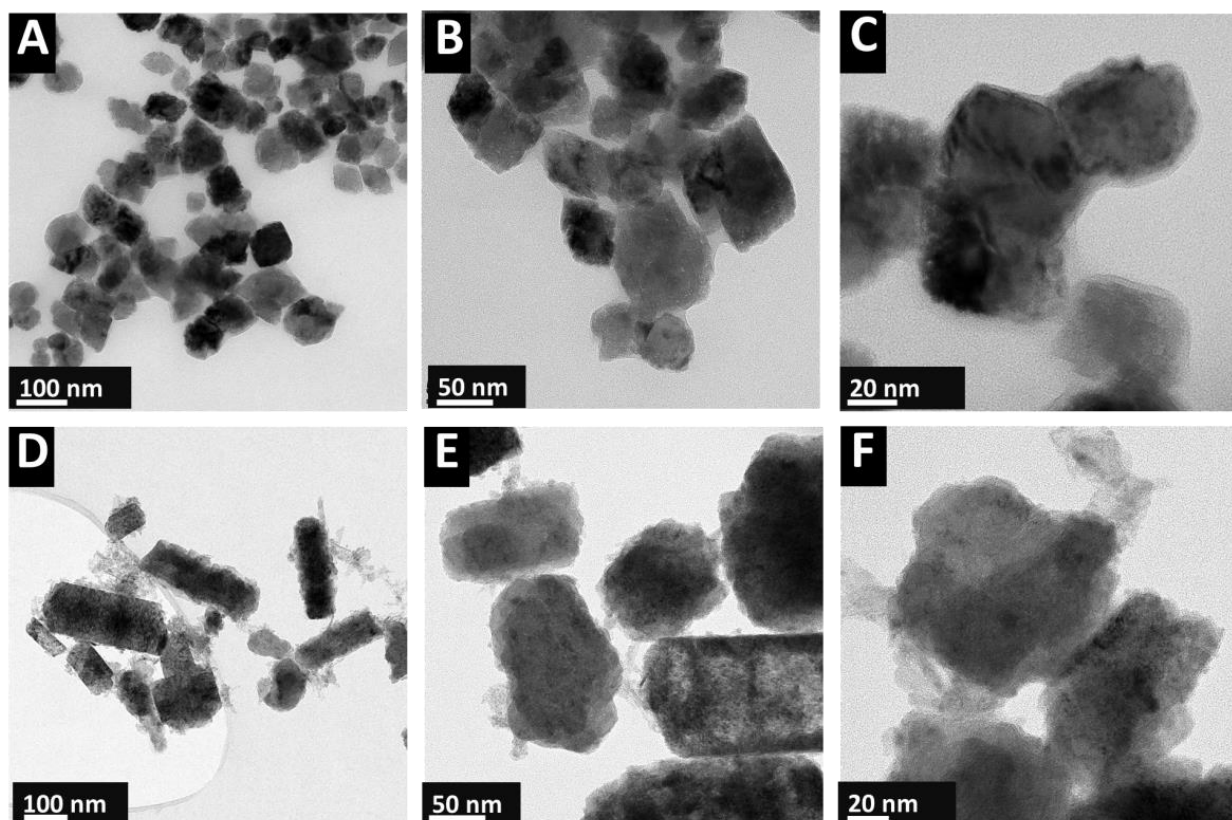


Figure 2. TEM images at different magnifications for (A–C) Mn-PEI and (D–F) Mn-MG powders.

The TEM images of Mn-PEI showed nanoparticles with a typical size of 50–70 nm. The particles show a nearly cubic shape. The low particle agglomeration is beneficial for their mixing with conductive carbon nanotubes and fabrication of electrodes. The TEM images of Mn-MG particles at different magnifications showed nearly cubic nanoparticles and nanorods with a small aspect ratio of 2–4. The TEM images also revealed the formation of particles of irregular shape. The length of the nanorods was in the range of 100–300 nm.

X-ray diffraction studies of Mn-PEI in Figure 3a, showed peaks of Mn_3O_4 , corresponding to JCPDS file 04-007-1841. The X-ray diffraction pattern of Mn-MG in Figure 3b, showed small peaks of Mn_3O_4 and $\alpha\text{-MnO}_2$, corresponding to JCPDS files 04-007-1841 and 44-0141, respectively. Mn-MG also contained an amorphous phase. The difference in sample composition was also confirmed by the results of the XPS investigations.

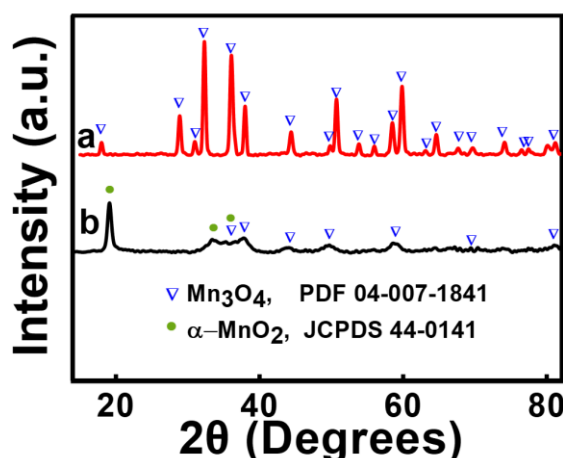


Figure 3. X-ray diffraction patterns of Mn-PEI and Mn-MG.

Figure 4 shows the results of the XPS studies of Mn-PEI and Mn-MG. XPS analysis showed the different oxidation states of Mn, such as Mn^{2+} , Mn^{3+} , and Mn^{4+} , in both materials. The high resolution XPS spectrum of Mn 2p showed two peaks which represent 2p_{3/2} and 2p_{1/2} orbitals, respectively. The splitting widths between the Mn 2p_{1/2} and Mn 2p_{3/2} peaks were 11.8 and 11.6 eV for Mn-PEI and Mn-MG, respectively. Testing results confirmed the mixed oxidation states of Mn-PEI and Mn-MG were in agreement with previously reported data for manganese oxides prepared by different methods [36–38]. However, the Mn-MG sample showed noticeably higher contents of Mn^{3+} and Mn^{4+} ions than Mn-PEI.

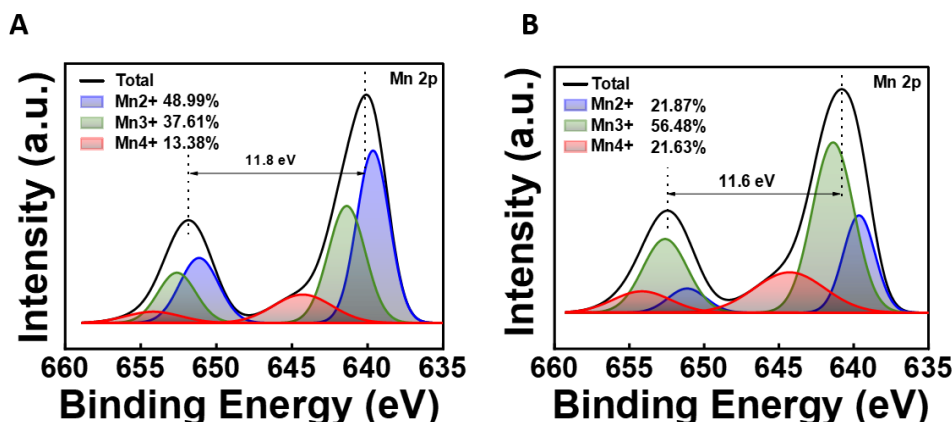
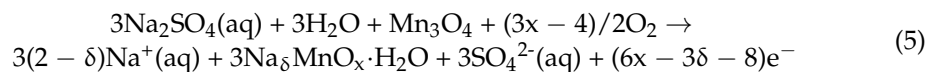


Figure 4. XPS spectra of as-synthesized (A) Mn-PEI and (B) Mn-MG in Mn 2p range.

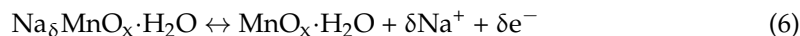
The results of the TEM, XRD, and XPS studies showed differences in the morphology, phase content, and oxidation state of Mn for Mn-PEI and Mn-MG. The differences can be

attributed to the effect of PEI and MG on particle synthesis. The amino groups of PEI and MG facilitated the adsorption of such molecules on manganese oxide particles. It should be noted that MG is a relatively small organic molecule, which has one secondary amino group, whereas PEI is a large polyelectrolyte molecule, which contains primary and secondary amino groups. Therefore, the size of the molecules and the interactions of primary and secondary amino groups with Mn atoms can exert influence on the synthesis of manganese oxide particles. The small size of the Mn-PEI and Mn-MG particles is beneficial for their application in supercapacitor electrodes. The small particle size offers advantages of a large surface area for electrolyte access. However, not all the surface area of the particles is available for electrolyte access. Previous studies showed that some particles with a high BET surface area exhibited lower capacitance, compared to other particles with a lower BET surface area [39–41]. It was demonstrated that small pores accessible by N₂ molecules in the BET experiments are not accessible by the solvated electrolyte ions [39–41]. It was concluded that capacitance was independent on the BET surface area [39–41].

It is suggested that the small particle size could be beneficial for the acceleration of the electrode activation. The activation step of Mn₃O₄ involves solvation and partial anodic oxidation [11]:



The oxidation of Mn₃O₄ during the activation process was confirmed by XPS and scanning transmission X-ray microscopy [11,14,15]. The capacitance increase during the electrode activation process was linked to the formation of an oxidized layer on the particle surface, which exhibited pseudocapacitive properties. The charge–discharge behavior is described by the following equation [11]:



The larger content of Mn³⁺ and Mn⁴⁺ in Mn-MG, compared to Mn-PEI, can potentially accelerate or eliminate the time-consuming oxidation and activation of electrode material in Reaction (5).

Mn-PEI and Mn-MG were used for the fabrication of composite electrodes containing MWCNT as conductive additives. The EDX studies showed a relatively uniform distribution of Mn and O in the electrodes. Electrochemical testing resulted in the incorporation of Na and S to the electrode from the electrolyte (Supplementary Materials, Figures S1–S4). Figure 5A,B shows CVs at different sweep rates for the Mn-PEI and Mn-MG electrodes for CP1. Both electrodes showed nearly rectangular CVs. However, Mn-MG showed higher currents, which indicated higher capacitance. Figure 5C,D shows CVs at a sweep rate of 10 mV s⁻¹ for CPs1–5. Mn-PEI showed a significant increase in the CV area in the order CP1 < CP2 < CP3. The area of CV was nearly the same for CP3–CP5. The increase in the CV area during the first CPs was related to electrode activation. However, the area of CV for Mn-MG was nearly the same for CPs1–5. Figure 5E compares the capacitances for CPs1–5 derived from the CV data for Mn-PEI. The capacitance for CP1 at a sweep rate of 1 mV s⁻¹ was found to be 1.92 F cm⁻² (48 F g⁻¹). The capacitance increased with the increasing sweep rate from 1 to 20 mV s⁻¹, showed a maximum, and then decreased to the value of 1.82 F cm⁻² (45.6 F g⁻¹) at 100 mV s⁻¹. The capacitance increase was attributed to electrode activation. The decrease in capacitance with the increasing scan rate above 20 mV s⁻¹ was due to limited diffusion and poor electrolyte access to the electrode surface at fast sweep rates.

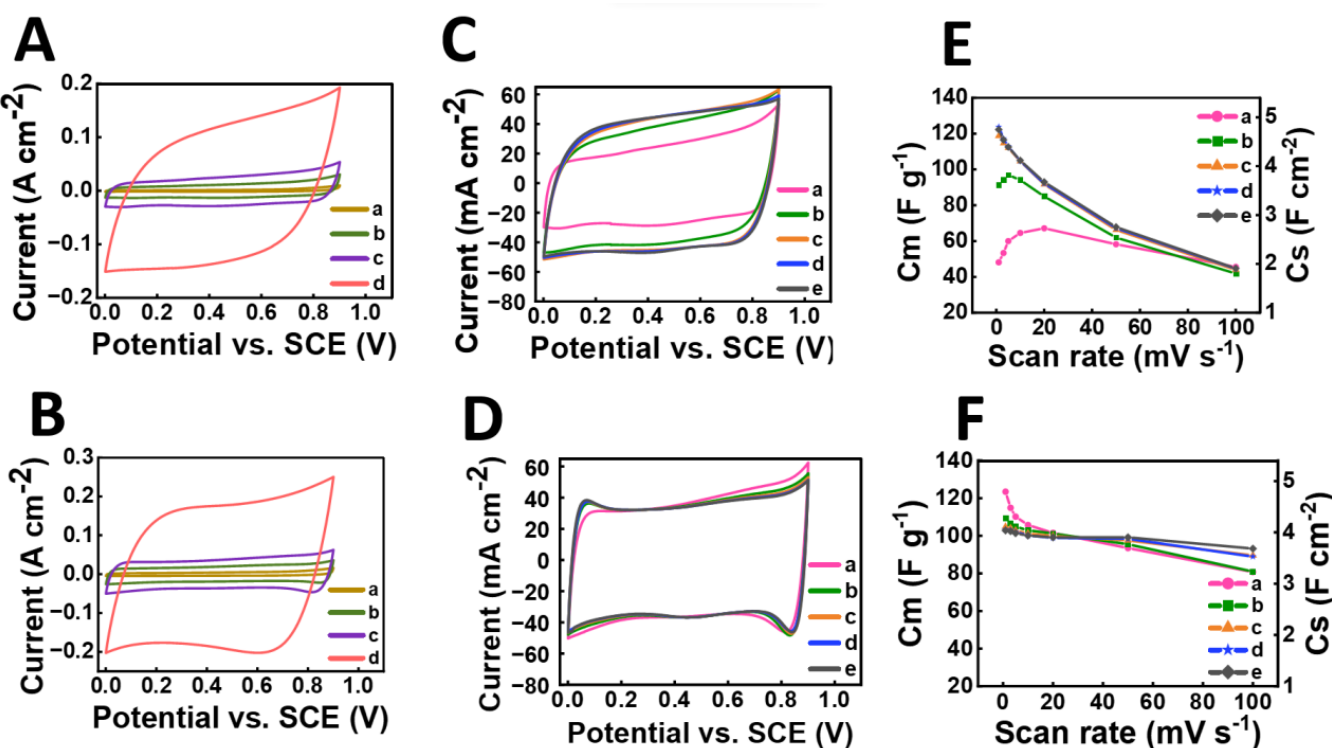


Figure 5. (A,B) CVs for (A) Mn–PEI and (B) Mn–MG at sweep rates of (a) 1, (b) 5, (c) 10, and (d) 50 mV s^{-1} for CP 1, (C,D) CVs at a sweep rate of 10 mV s^{-1} for (C) Mn–PEI, (D) Mn–MG, and (a) CP1, (b) CP2, (c) CP3, (d) CP4, (e) CP5, (E,F) capacitance versus sweep rate for (E) Mn–PEI, (F) Mn–MG, and (a) CP1, (b) CP2, (c) CP3, (d) CP4, (e) CP5.

The activation of Mn-PEI resulted in an increased capacitance of 3.64 F cm^{-2} (91.14 F g^{-1}) for CP2 at 1 mV s^{-1} , compared to CP1. The capacitance showed a small maximum and decreased to the value of 1.67 (41.86 F g^{-1}) F cm^{-2} at 100 mV s^{-1} .

CP3 showed a further increase in capacitance; however, the capacitance values remained unchanged for CPs3–5. For CP5, the capacitance at 1 mV s^{-1} was found to be 4.89 F cm^{-2} (122.26 F g^{-1}) and it decreased to 1.79 F cm^{-2} (44.75 F g^{-1}) at 100 mV s^{-1} . The capacitance retention in the range of 1 – 100 mV s^{-1} was 36.6%.

Investigations of Mn-MG (Figure 5F) showed capacitances of 4.88 F cm^{-2} (123.47 F g^{-1}) at 1 mV s^{-1} , which decreased to the value of 3.19 F cm^{-2} (80.76 F g^{-1}) at 100 mV s^{-1} for CP1. A capacitance reduction for sweep rates 1 – 10 mV s^{-1} and capacitance increase for sweep rates 50 – 100 mV s^{-1} was observed for CP2. The capacitance remained unchanged for CPs3–5. The capacitance was found to be 4.06 F cm^{-2} (102.87 F g^{-1}) and 3.68 F cm^{-2} (93.19 F g^{-1}) for sweep rates of 1 and 100 mV s^{-1} , respectively. Mn-MG showed a remarkably high capacitance retention of 90.6% in the range 1 – 100 mV s^{-1} . High capacitance retention and high capacitance at high sweep rates are important for applications of Mn-MG in the cathodes of supercapacitor devices with enhanced power–energy characteristics. It should be noted that $C_s(C_m)$ at 100 mV s^{-1} for Mn-MG is significantly higher than the corresponding values for Mn_3O_4 and MnO_2 electrodes of a similar mass reported in the literature [14,15,42]. Moreover, the activation procedure can be practically eliminated for Mn-MG. This contrasts with previous investigations of electrodes of similar mass [11,14,15], which showed significant capacitance variations during CPs1–5. The difference in cycling behavior of Mn-PEI and Mn-MG can result from the relatively large size of PEI macromolecules, which can provide insulating layers, resulting in longer activation. The capacitive properties of Mn-MG and Mn-PEI electrodes are attributed to the pseudocapacitive charge storage mechanism of the manganese oxide, described by Reaction (6). The contribution of the electrical double-layer capacitance of multiwalled carbon nanotubes was negligibly small

due to their low specific capacitance and small content in the composite electrode. As pointed out above, multiwalled carbon nanotubes were used as conductive additives.

Figure 6 and Figure S5 show the EIS data for the Mn-PEI and Mn-MG electrodes. The Nyquist plots (Figure 6A,B) indicated good pseudocapacitive behavior and low resistance of the electrodes. The frequency dependences of the real and imaginary components of a complex capacitance are presented in Figure 6C–F. The analysis of the EIS data for Mn-PEI showed a variation in the impedance and complex capacitance for testing after CPs1–3. The increase in the real component of capacitance was attributed to electrode activation. This is in agreement with the CV data. The relaxation frequency, corresponding to the maximum in the frequency dependence of the imaginary component of capacitance, decreased after cycling. This indicated a reduction in capacitance retention.

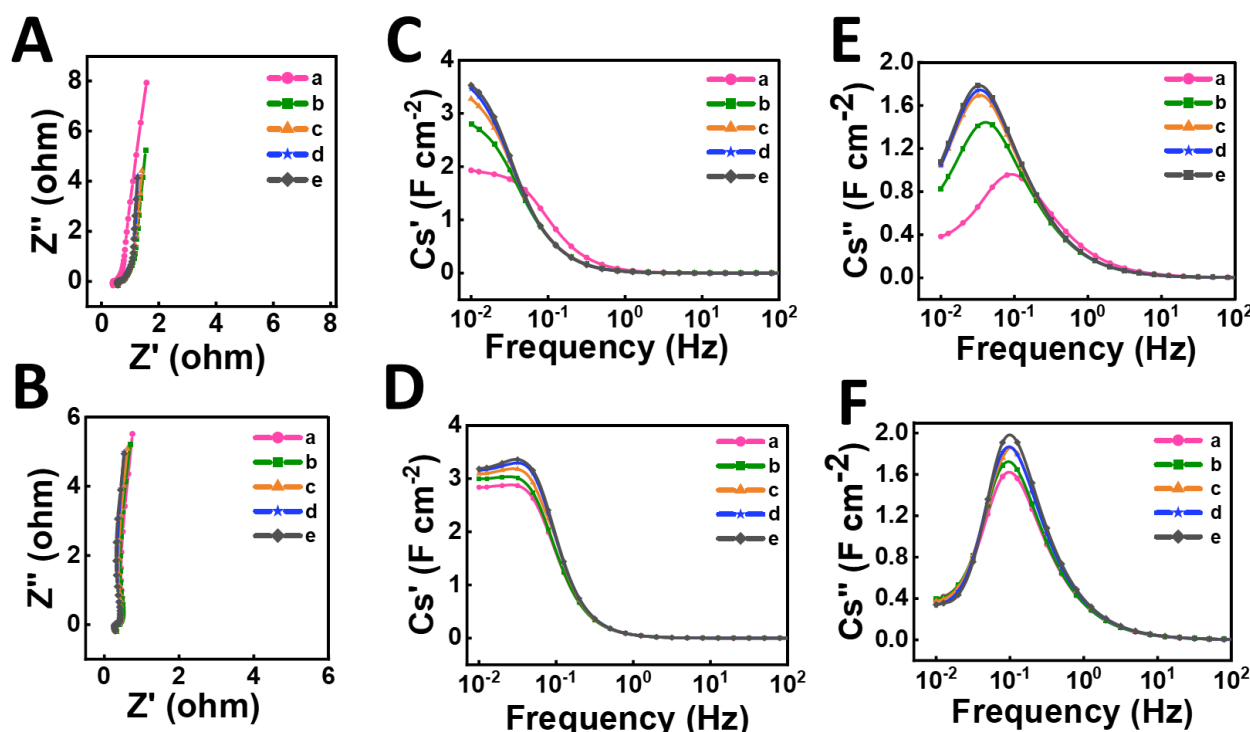


Figure 6. (A,B) Nyquist plots, (C,D) real components of complex capacitance, (E,F) imaginary components of complex capacitance for (A,C,E) Mn-PEI and (B,D,F) Mn-MG after (a) CP1, (b) CP2, (c) CP3, (d) CP4, (e) CP5.

The EIS data for Mn-MG showed only small variations in the impedance and components of AC capacitance during cycling. This indicated that the electrode activation procedure can be practically eliminated. In contrast to Mn-PEI, the relaxation frequency showed a slight increase during cycling and remained relatively high after CP5. This result is in agreement with the CV data, providing additional evidence of enhanced capacitance retention at fast electrode charging/discharging. The EIS data were also analyzed using an equivalent circuit simulation with ZSimpWin software. Figure 7A presents the EIS experimental data and simulation for Mn-PEI and Mn-MG. The equivalent circuit developed for high active mass bulk electrodes [42] was used. However, in contrast to [42], the circuit (Figure 7B) did not include Warburg impedance, which was negligibly small for the developed electrodes. The simulation results agreed with the experimental data. The Mn-MG electrodes showed a charge-transfer resistance (R_{CT}) of 0.33 Ohm, which is lower than the $R_{CT} = 0.43$ Ohm for Mn-PEI. Therefore, the CV and EIS data for Mn-MG show a small influence of ion diffusion on the pseudocapacitive properties, which resulted in good capacitance retention at high scan rates and negligibly small Warburg impedance.

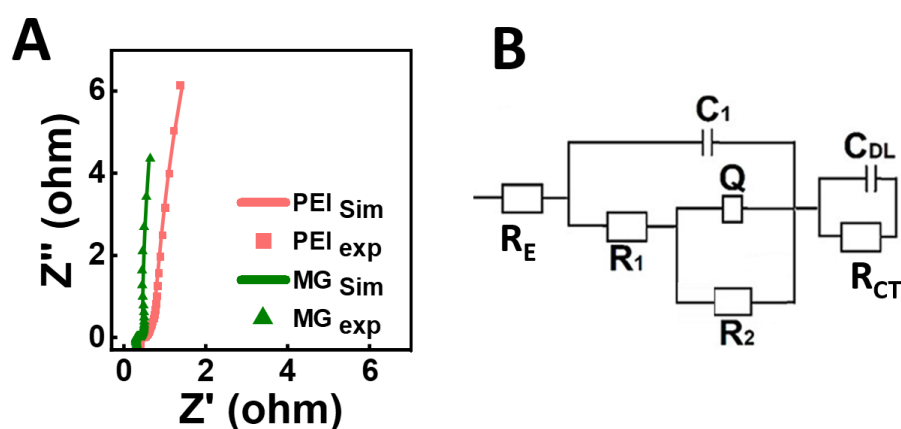


Figure 7. (A) EIS results (Nyquist plot) of the experimental data (exp) and simulation data (sim) for Mn-PEI and Mn-MG, (B) the equivalent circuit used for simulation study.

Figure 8 compares the GCD data for Mn-PEI and Mn-MG. The nearly linear charge-discharge curves indicated good pseudocapacitive properties of the electrodes. The capacitance of Mn-PEI decreased from 5.03 F cm^{-2} (125.87 F g^{-1}) to 4.17 F cm^{-2} (104.49 F g^{-1}) with an increasing current density from 3 to 40 mA cm^{-2} and showed a capacitance retention of 82.9% in this current density range. The capacitance of the Mn-MG electrodes was found to be 4.33 F cm^{-2} (109.57 F g^{-1}) at 3 mA cm^{-2} . It decreased to 4.00 F cm^{-2} (101.25 F g^{-1}) with an increasing current density to 40 mA cm^{-2} . The Mn-MG electrodes showed a capacitance retention of 92.4%.

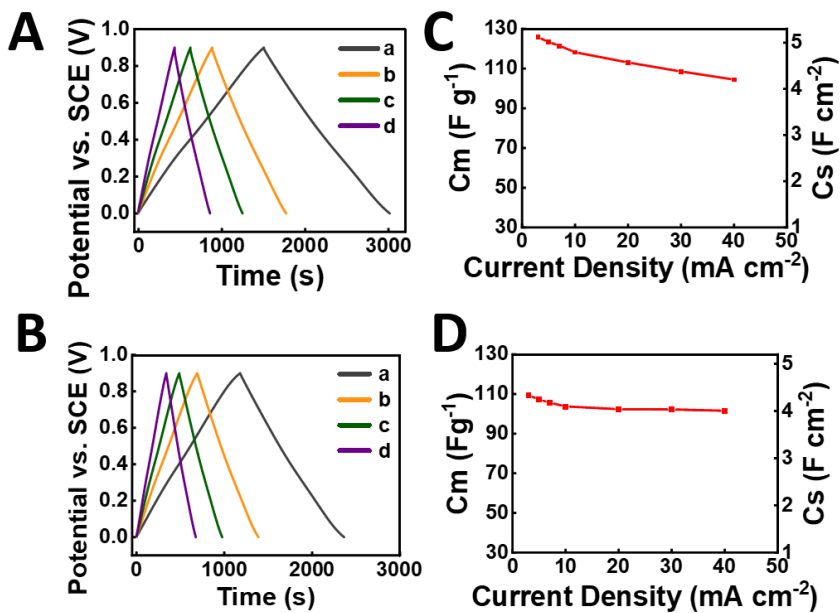


Figure 8. (A,B) GCD data for (A) Mn-PEI and (B) Mn-MG at current densities of (a) 3, (b) 5, (c) 7, and (d) 10 mA cm^{-2} and (C,D) capacitance versus current density calculated from the GCD data for (C) Mn-PEI and (D) Mn-MG.

Figure 9 shows the cycling behavior of the as-prepared Mn-PEI and Mn-MG electrodes. The Mn-PEI electrodes showed a significant capacitance variation of about 380% for the first 500 cycles and a very small capacitance change during further cycling. The capacitance increased from 23.0 to 86.1 F g^{-1} during cycling. The Mn-MG electrodes showed a 20% increase in capacitance during the first 220 cycles and after that, the capacitance was practically unchanged during cycling. The capacitance increased from 83.3 F g^{-1} to 96.7 F g^{-1} during cycling. The analysis of the cycling behavior presents additional evidence of

acceleration of the activation procedure for Mn-MG, compared to Mn-PEI. Turning again to the XPS data, it is seen that the higher oxidation state of Mn in Mn-MG eliminates the need for electrochemical oxidation and facilitates the activation process. It should be noted that electrode acceleration is influenced by a scan rate. The electrode material oxidation time during an individual cycle decreases with the increasing scan rate and a larger number of cycles are required for the electrochemical oxidation. Electrochemical cycling resulted in some changes in the electrode microstructure. The comparison of the SEM images of the electrode microstructure before and after cycling (Figure S6) showed that cycling resulted in increasing microporosity, which was beneficial for electrolyte transport.

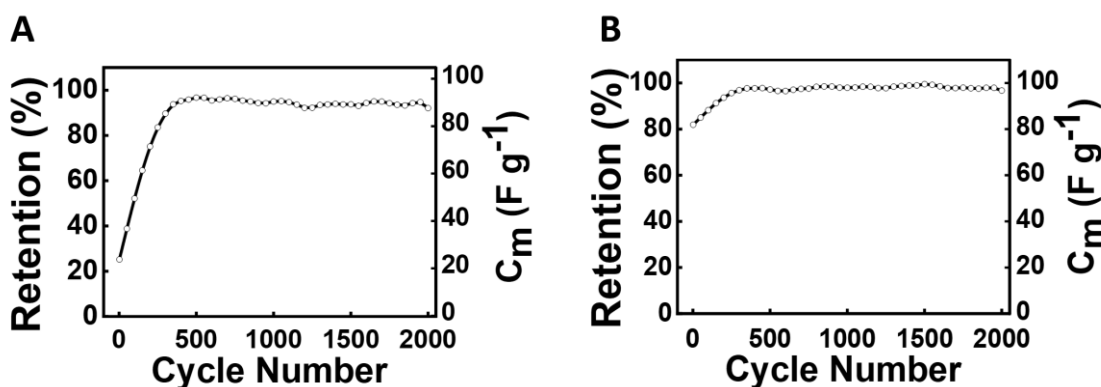


Figure 9. Capacitance retention and capacitance versus CV cycle number at a scan rate of 50 mV s^{-1} for (A) Mn-PEI and (B) Mn-MG electrodes. Retention represents capacitances at different cycle numbers normalized by the capacitance for cycle 2000.

The results of CV, EIS, and GCD indicate a remarkable capacitance retention of Mn-MG electrodes. The ability to retain high capacitance at high charge-discharge rates is critically important for the development of high-power supercapacitors. Of particular importance is the ability to accelerate and practically eliminate the electrode activation procedure. It is in this regard that in previous investigations, the capacitance increased by three times during the activation procedure [14]. This makes Mn-MG a material of choice for advanced supercapacitors and a promising alternative to the most developed MnO_2 cathodes. It should be noted that MnO_2 shows capacitance variation during initial cycling [19]. Another difficulty is related to the high resistivity of MnO_2 , which results in poor capacitance retention at high charge-discharge rates. The progress in the development of MnO_2 -based electrodes is limited due to the use of permanganate precursors, which oxidize and decompose organic capping agents and other processing additives. The use of Mn_3O_4 offers advantages due to the ability to modify its properties [43] by doping and forming spinel solid solutions with other chemical elements and the ability to synthesize nanoparticles in the presence of organic alkalizers and dispersants from Mn^{2+} salt precursors, which are chemically compatible with organic chemical-processing additives.

It is important to note that good electrochemical performance was achieved at high active mass loading, which is a key factor for the fabrication of electrodes with high areal capacitance [19]. The comparison with the literature data for Mn_3O_4 electrodes with high active mass loadings indicates that our approach offers benefits of high areal capacitance, excellent capacitance retention at high charge-discharge rates, and low impedance [11,14,15,19]. Another important advancement was the acceleration and practical elimination of the time-consuming electrode activation procedure [11,14], which is important for practical applications.

4. Conclusions

This investigation demonstrated the feasibility of manganese oxide synthesis from $\text{Mn}(\text{NO}_3)_2$ solutions using PEI and MG as environmentally friendly pH modifiers and dispersants for synthesis. In this new approach, the use of inorganic alkalis for hydrothermal synthesis was avoided. The method facilitated the synthesis of manganese oxide

nanoparticles. The approach developed in this investigation can potentially be used for the manufacturing of other nanomaterials for energy storage devices. The method of electrode material fabrication offers the benefit of accelerated electrode activation procedure, which was practically eliminated for the Mn-MG electrodes. The problem of poor capacitance retention and low capacitance of manganese oxide electrodes was successfully addressed. The Mn-MG electrodes showed a remarkably high capacitance of 3.68 F cm^{-2} (93.19 F g^{-1}) at a sweep rate of 100 mV s^{-1} and a high capacitance retention of 90.6% in the CV sweep range of $1\text{--}100 \text{ mV s}^{-1}$. Mn-MG electrodes are promising for the development of high-power supercapacitors.

Supplementary Materials: The following supporting information can be downloaded at: <https://www.mdpi.com/article/10.3390/batteries9070365/s1>; Figure S1: EDX data for Mn-PEI electrodes before electrochemical testing.; Figure S2: EDX data for Mn-PEI electrodes after electrochemical testing.; Figure S3: EDX data for Mn-MG electrodes before electrochemical testing.; Figure S4: EDX data for Mn-MG electrodes after electrochemical testing.; Figure S5: (A,B) magnified Nyquist plots for (A) Mn-PEI and (B) Mn-MG respectively after (a) CP1, (b) CP2, (c) CP3, (d) CP4, (e) CP5.; Figure S6: SEM images of microstructure for (A,B) fresh and tested Mn-PEI electrode, respectively and (C,D) fresh and tested Mn-MG electrode, respectively.

Author Contributions: Conceptualization, M.A., M.N. and I.Z.; methodology, M.A. and I.Z.; software, M.A.; validation, M.A., M.N. and I.Z.; formal analysis, M.A., M.N. and I.Z.; investigation, M.A. and I.Z.; resources, M.A., M.N. and I.Z.; data curation, M.A. and M.N.; writing—original draft preparation, M.A., M.N. and I.Z.; writing—review and editing, M.A., M.N. and I.Z.; visualization, M.A., M.N. and I.Z.; supervision, I.Z.; project administration, M.N. and I.Z.; funding acquisition, I.Z. All authors have read and agreed to the published version of the manuscript.

Funding: This research was funded by the Natural Sciences and Engineering Research Council of Canada, grant number RGPIN-2018-04014, and CRC program.

Data Availability Statement: Data are available within the article and Supplementary Materials.

Acknowledgments: Electron microscopy investigations were performed at the Canadian Centre for Electron Microscopy.

Conflicts of Interest: The authors declare no conflict of interest. The funders had no role in the design of the study; in the collection, analyses, or interpretation of data; in the writing of the manuscript, or in the decision to publish the results.

References

1. Liao, Y.; Yang, C.; Xu, Q.; Zhao, W.; Zhao, J.; Wang, K.; Chen, H.-C. Ag-Doping Effect on MnO_2 Cathodes for Flexible Quasi-Solid-State Zinc-Ion Batteries. *Batteries* **2022**, *8*, 267. [[CrossRef](#)]
2. Li, Z.; Ji, C.; Guo, F.; Mi, H.; Zhu, X.; Qiu, J. A multi-interface CoNi-SP/C heterostructure for quasi-solid-state hybrid supercapacitors with a graphene oxide-containing hydrogel electrolyte. *J. Mater. Chem. A* **2022**, *10*, 4671–4682. [[CrossRef](#)]
3. Wang, M.; Liu, X.; Wu, X. Surface Selenization of NiCo-Layered Double Hydroxide Nanosheets for High-Performance Supercapacitors. *Batteries* **2023**, *9*, 49. [[CrossRef](#)]
4. Cevik, E.; Gunday, S.T.; Akhtar, S.; Yamani, Z.H.; Bozkurt, A. Sulfonated hollow silica spheres as electrolyte store/release agents: High-performance supercapacitor applications. *Energy Technol.* **2019**, *7*, 1900511. [[CrossRef](#)]
5. Liang, J.; Zhao, H.; Yue, L.; Fan, G.; Li, T.; Lu, S.; Chen, G.; Gao, S.; Asiri, A.M.; Sun, X. Recent advances in electrospun nanofibers for supercapacitors. *J. Mater. Chem. A* **2020**, *8*, 16747–16789. [[CrossRef](#)]
6. Cao, Y.; Liang, J.; Li, X.; Yue, L.; Liu, Q.; Lu, S.; Asiri, A.M.; Hu, J.; Luo, Y.; Sun, X. Recent advances in perovskite oxides as electrode materials for supercapacitors. *Chem. Commun.* **2021**, *57*, 2343–2355. [[CrossRef](#)]
7. Ma, X.; Chen, J.; Yuan, B.; Li, Y.; Yu, L.; Zhao, W. Three-dimensional hollow nickel phosphate microspheres with controllable hoyia-like structure for high-performance enzymeless glucose detection and supercapacitor. *Appl. Surf. Sci.* **2022**, *588*, 152928. [[CrossRef](#)]
8. Alqarni, A.N.; Cevik, E.; Gondal, M.; Almessiere, M.; Baykal, A.; Bozkurt, A.; Slimani, Y.; Hassan, M.; Iqbal, A.; Alotaibi, S.A. Synthesis and design of vanadium intercalated spinal ferrite ($\text{Co}_{0.5}\text{Ni}_{0.5}\text{V}_{x}\text{Fe}_{1.6-x}\text{O}_4$) electrodes for high current supercapacitor applications. *J. Energy Storage* **2022**, *51*, 104357. [[CrossRef](#)]
9. Lin, S.; Yang, F.; Yang, Z.; Wang, J.; Xiang, L. Preparation of Hydrated TiO_2 Particles by Hydrothermal Hydrolysis of Mg/Al-Bearing TiOSO_4 Solution. *Nanomaterials* **2023**, *13*, 1179. [[CrossRef](#)]

10. Mineo, G.; Scuderi, M.; Pezzotti Escobar, G.; Mirabella, S.; Bruno, E. Engineering of Nanostructured WO₃ Powders for Asymmetric Supercapacitors. *Nanomaterials* **2022**, *12*, 4168. [[CrossRef](#)]
11. Yang, W.; Eraky, H.; Zhang, C.; Hitchcock, A.P.; Zhitomirsky, I. Scanning transmission X-ray microscopy studies of electrochemical activation and capacitive behavior of Mn₃O₄ supercapacitor electrodes. *J. Mater. Chem. A* **2022**, *10*, 18267–18277. [[CrossRef](#)]
12. Gagrani, A.; Ding, B.; Wang, Y.; Tsuzuki, T. pH dependent catalytic redox properties of Mn₃O₄ nanoparticles. *Mater. Chem. Phys.* **2019**, *231*, 41–47. [[CrossRef](#)]
13. Kosmulski, M. Isoelectric points and points of zero charge of metal (hydr)oxides: 50 years after Parks' review. *Adv. Colloid Interface Sci.* **2016**, *238*, 1–61. [[CrossRef](#)]
14. Poon, R.; Zhitomirsky, I. High areal capacitance of Mn₃O₄-carbon nanotube electrodes. *Mater. Lett.* **2018**, *215*, 4–7. [[CrossRef](#)]
15. Milne, J.; Zhitomirsky, I. Application of octanohydroxamic acid for liquid-liquid extraction of manganese oxides and fabrication of supercapacitor electrodes. *J. Colloid Interface Sci.* **2018**, *515*, 50–57. [[CrossRef](#)]
16. Shar, S.S.; Cevik, E.; Bozkurt, A.; Yaman, C.; Almutari, Z.; Kayed, T.S. Molybdate incorporated poly (acrylic acid) electrolytes for use in quasi-solid state carbon based supercapacitors: Redox-active polychelates. *Electrochim. Acta* **2020**, *354*, 136770. [[CrossRef](#)]
17. Cevik, E.; Gunday, S.T.; Bozkurt, A.; Amine, R.; Amine, K. Bio-inspired redox mediated electrolyte for high performance flexible supercapacitor applications over broad temperature domain. *J. Power Sources* **2020**, *474*, 228544. [[CrossRef](#)]
18. Cevik, E.; Gunday, S.T.; Iqbal, A.; Akhtar, S.; Bozkurt, A. Synthesis of hierarchical multilayer N-doped Mo₂C@MoO₃ nanostructure for high-performance supercapacitor application. *J. Energy Storage* **2022**, *46*, 103824. [[CrossRef](#)]
19. Chen, R.; Yu, M.; Sahu, R.P.; Puri, I.K.; Zhitomirsky, I. The development of pseudocapacitor electrodes and devices with high active mass loading. *Adv. Energy Mater.* **2020**, *10*, 1903848. [[CrossRef](#)]
20. Gutiérrez, G.L.; Dávila, O.O.; Aguilar, C.L.; Jiménez, M.D.; González, R.S.; Sirés, I.; Brillas, E.; Fabregat-Safont, D.; Navarro, A.R.; Arandes, J.B. Electrochemical oxidation of meglumine in a pharmaceutical formulation using a nanocomposite anode. *Electrochim. Acta* **2023**, *437*, 141457. [[CrossRef](#)]
21. Fusina, A.; Degot, P.; Touraud, D.; Kunz, W.; Nardello-Rataj, V. Enhancement of water solubilization of quercetin by meglumine and application of the solubilization concept to a similar system. *J. Mol. Liq.* **2022**, *368*, 120756. [[CrossRef](#)]
22. Hussien, M.A.; Essa, E.; El-Gizawy, S.A. Investigation of the effect of formulation additives on telmisartan dissolution rate: Development of oral disintegrating tablets. *Eur. J. Biomed. Pharm. Sci.* **2019**, *6*, 12–20.
23. Parikh, B.; Patel, D.; Patel, C.; Dave, J.; Gothi, G.; Patel, T. Formulation optimization and evaluation of immediate release tablet of telmisartan. *J. Glob. Pharma Technol.* **2010**, *2*, 79–84.
24. Dong, L.; Mai, Y.; Liu, Q.; Zhang, W.; Yang, J. Mechanism and improved dissolution of glycyrrhetic acid solid dispersion by alkalizers. *Pharmaceutics* **2020**, *12*, 82. [[CrossRef](#)]
25. Manley, K.; Bravo-Nuevo, A.; Minton, A.R.; Sedano, S.; Marcy, A.; Reichman, M.; Tobia, A.; Artlett, C.M.; Gilmour, S.K.; Laury-Kleintop, L.D. Preclinical study of the long-range safety and anti-inflammatory effects of high-dose oral meglumine. *J. Cell. Biochem.* **2019**, *120*, 12051–12062. [[CrossRef](#)]
26. Palchevska, T.; Saliy, O.; Baula, O.; Palchevskyi, K.; Onishchuk, O. The role of excipients of trometamolum and meglumine in the formation of biopharmaceutical properties of medicinal products of various pharmacites. *Farmatsevtichnyi Zhurnal* **2021**, *4*, 64–75. [[CrossRef](#)]
27. Sawamura, T.; Okuyama, M.; Maeda, H.; Obata, A.; Kasuga, T. Preparation of calcium-phosphate cements with high compressive strength using meglumine as a water reducer. *J. Ceram. Soc. Jpn.* **2016**, *124*, 223–228. [[CrossRef](#)]
28. Guo, R.-Y.; An, Z.-M.; Mo, L.-P.; Wang, R.-Z.; Liu, H.-X.; Wang, S.-X.; Zhang, Z.-H. Meglumine: A novel and efficient catalyst for one-pot, three-component combinatorial synthesis of functionalized 2-amino-4-H-pyrans. *ACS Comb. Sci.* **2013**, *15*, 557–563. [[CrossRef](#)]
29. Sravya, G.; Suresh, G.; Zyryanov, G.V.; Balakrishna, A.; Madhu Kumar Reddy, K.; Suresh Reddy, C.; Venkataramaiah, C.; Rajendra, W.; Bakthavatchala Reddy, N. A meglumine catalyst-based synthesis, molecular docking, and antioxidant studies of dihydropyrano [3,2-b] chromenedione derivatives. *J. Heterocycl. Chem.* **2020**, *57*, 355–369. [[CrossRef](#)]
30. Benjaminsen, R.V.; Mattebjerg, M.A.; Henriksen, J.R.; Moghimi, S.M.; Andresen, T.L. The possible “proton sponge” effect of polyethylenimine (PEI) does not include change in lysosomal pH. *Mol. Ther.* **2013**, *21*, 149–157. [[CrossRef](#)]
31. Tang, F.; Uchikoshi, T.; Ozawa, K.; Sakka, Y. Effect of polyethylenimine on the dispersion and electrophoretic deposition of nano-sized titania aqueous suspensions. *J. Eur. Ceram. Soc.* **2006**, *26*, 1555–1560. [[CrossRef](#)]
32. Zhu, X.; Tang, F.; Suzuki, T.S.; Sakka, Y. Role of the initial degree of ionization of polyethylenimine in the dispersion of silicon carbide nanoparticles. *J. Am. Ceram. Soc.* **2003**, *86*, 189–191. [[CrossRef](#)]
33. Dietrich, A.; Neubrand, A. Effects of particle size and molecular weight of polyethylenimine on properties of nanoparticulate silicon dispersions. *J. Am. Ceram. Soc.* **2001**, *84*, 806–812. [[CrossRef](#)]
34. Laarz, E.; Bergström, L. Dispersing WC-Co powders in aqueous media with polyethylenimine. *Int. J. Refract. Met. Hard Mater.* **2000**, *18*, 281–286. [[CrossRef](#)]
35. Rubianes, M.D.; Rivas, G.A. Dispersion of multi-wall carbon nanotubes in polyethylenimine: A new alternative for preparing electrochemical sensors. *Electrochim. Commun.* **2007**, *9*, 480–484. [[CrossRef](#)]
36. Wang, B.; Yu, J.; Lu, Q.; Xiao, Z.; Ma, X.; Feng, Y. Preparation of Mn₃O₄ microspheres via glow discharge electrolysis plasma as a high-capacitance supercapacitor electrode material. *J. Alloys Compd.* **2022**, *926*, 166775. [[CrossRef](#)]

37. Chen, J.; Chu, K.; Sun, S.; Chen, H.; Song, B.; Wang, J.; Liu, Z.; Zhu, L. Synthesis of magnetic core-shell $\text{Fe}_3\text{O}_4\text{-Mn}_3\text{O}_4$ composite for degradation of sulfadiazine via peroxymonosulfate activation: Characterization, mechanism and toxicity analysis. *J. Environ. Chem. Eng.* **2023**, *11*, 109230. [[CrossRef](#)]
38. He, L.; Zhang, G.; Dong, Y.; Zhang, Z.; Xue, S.; Jiang, X. Polyetheramide templated synthesis of monodisperse Mn_3O_4 nanoparticles with controlled size and study of the electrochemical properties. *Nano-Micro Lett.* **2014**, *6*, 38–45. [[CrossRef](#)]
39. Reddy, R.N.; Reddy, R.G. Sol-gel MnO_2 as an electrode material for electrochemical capacitors. *J. Power Sources* **2003**, *124*, 330–337. [[CrossRef](#)]
40. Jeong, Y.; Manthiram, A. Nanocrystalline manganese oxides for electrochemical capacitors with neutral electrolytes. *J. Electrochem. Soc.* **2002**, *149*, A1419. [[CrossRef](#)]
41. Dong, W.; Sakamoto, J.S.; Dunn, B. Electrochemical properties of vanadium oxide aerogels. *Sci. Technol. Adv. Mater.* **2003**, *4*, 3. [[CrossRef](#)]
42. Wang, Y.; Liu, Y.; Zhitomirsky, I. Surface modification of MnO_2 and carbon nanotubes using organic dyes for nanotechnology of electrochemical supercapacitors. *J. Mater. Chem. A* **2013**, *1*, 12519–12526. [[CrossRef](#)]
43. Barai, H.R.; Lopa, N.S.; Ahmed, F.; Khan, N.A.; Ansari, S.A.; Joo, S.W.; Rahman, M.M. Synthesis of Cu-Doped $\text{Mn}_3\text{O}_4@$ Mn-Doped CuO Nanostructured Electrode Materials by a Solution Process for High-Performance Electrochemical Pseudocapacitors. *ACS Omega* **2020**, *5*, 22356–22366. [[CrossRef](#)] [[PubMed](#)]

Disclaimer/Publisher's Note: The statements, opinions and data contained in all publications are solely those of the individual author(s) and contributor(s) and not of MDPI and/or the editor(s). MDPI and/or the editor(s) disclaim responsibility for any injury to people or property resulting from any ideas, methods, instructions or products referred to in the content.